In-situ measurement of texture development rate in $CaIrO_3$ post-perovskite

Simon A. Hunt[1], Andrew M. Walker[2], Elisabetta Mariani[3]

1. Department of Earth Sciences, University College London, Gower Street, London. WCE1 6BT United Kingdom
2. School of Earth and Environment, University of Leeds, Leeds. LS2 9JT United Kingdom
3. School of Environmental Sciences, Jane Herdman Laboratories, University of Liverpool. L69 3GP United Kingdom

Abstract

The rate of crystallographic preferred orientation (CPO) development during deformation of post-perovskite is crucial in interpreting seismic anisotropy in the lowermost mantle but the stability field of $MgSiO_3$ post-perovskite prevents high-strain deformation experiments being performed on it. Therefore, to constrain the rate of CPO development in post-perovskite, we deformed $CaIrO_3$, a low-pressure analogue of $MgSiO_3$ post-perovskite, in simple shear at 3.2 GPa and 400 °C to a shear strain (γ) of 0.81. From X-ray diffraction patterns acquired during deformation, we invert for CPO as a function of strain. By comparing the CPO that develops with visco-plastic self-consistent (VPSC) models we constrain the critical resolved shear stresses (CRSS) of the non-primary slip-systems in $CaIrO_3$ to be of order 6 times stronger than the primary [100](010) slip system. This value is significantly less than has been assumed by previous studies and if applicable to $MgSiO_3$ implies that seismic anisotropy in the D″ layer develops slower than has previously been assumed.

Keywords

Electron Back-Scatter diffraction (EBSD), Orientation Distribution Function (ODF), Lattice Preferred Orientation (LPO), inverse pole figure, D″ layer

1 Introduction

Analysis of the origin of the seismic anisotropy observed in the lowermost mantle (D″) offers the possibility of furthering our understanding of Earth's planetary scale dynamics (e.g. Panning and Romanowicz 2004, Merkel et al. 2007). However, this analysis is stymied by a lack of detailed constraints on the formation mechanisms of the anisotropy and its links with convectively driven deformation. Although other mechanisms are possible (Hall et al. 2004, Nowacki et al. 2011), the leading hypothesis is that seismic anisotropy is generated by dislocation accommodated deformation of $MgSiO_3$ post-perovskite (Oganov and Ono 2004, Murakami et al. 2004, Wookey et al. 2005b). Because dislocations are constrained to move on particular glide planes, such deformation results in a rotation of the lattice of the individual crystals forming the rocky lowermost mantle and the generation of a non-uniform crystallographic (or lattice) preferred orientation (CPO). This, in turn, imparts elastic anisotropy on the polycrystalline lowermost mantle. The effect of this anisotropy can be detected by measuring shear wave splitting in combinations of *S*, S_{diff}, *ScS*, *SKS* or *SKKS* phases (Lay and Young 1991, Vinnik et al. 1995,

Kendall and Silver 1996, Wookey et al. 2005a, Rokosky et al. 2006, Wookey and Kendall 2008, Long 2009, He and Long 2011, Lynner and Long 2012, 2014, Nowacki et al. 2010, Ford et al. 2015), in anisotropic compressional and shear wave tomography (Panning and Romanowicz 2004, 2006, Kustowski et al. 2008, Boschi and Dziewonski 2000, Soldati et al. 2003), or as splitting of the Earth's normal modes (Montagner and Kennett 1996, Beghein et al. 2006, Koelemeijer et al. 2012). Ultimately, we should be able to relate these observations to mantle flow in D″, linking seismology to geodynamics.

The link between mantle flow and seismic anisotropy can be made by forward modelling of deformation in polycrystalline aggregates representative of the lowermost mantle. The forward model uses a candidate flow field to provide the macroscopic strain rate, a method to describe the interactions between adjacent deforming grains, and information about how individual grains deform. Examples of such modelling include studies where mantle flow is driven by a two or three-dimensional simulation of convection in the mantle (Wenk et al. 2011, Cottaar et al. 2014), and others where the flow field is derived from the inversion of present-day geophysical observations (Walker et al. 2011, Nowacki et al. 2013). Results are then compared to shear wave splitting (Nowacki et al. 2013, Cottaar et al. 2014) or tomographic data (Walker et al. 2011).

Arguably, the biggest uncertainly in current forward modelling of CPO generation in the D″ is the description of post-perovskite single crystal deformation mechanisms. For dislocation mitigated deformation, this consists of the resolved stress needed to cause motion of a dislocation belonging to each slip system of the crystal. The slip system with the lowest critical resolved shear stress (CRSS, τ_0) tends to control the overall patterns of CPO and seismic anisotropy and is the parameter most easily constrained by experiment. The ratio of CRSS between different slip systems is not as readily constrained but these ratios define the plastic anisotropy and rate of CPO development. All else being equal, a material with higher plastic anisotropy will develop a strong CPO after less strain than a material with more similar values for the CRSS of each slip system and lower plastic anisotropy. For example, in quartz the texture caused by deformation varies with temperature, and modelling shows that this can be explained by variation in the CRSS ratios and thus the plastic anisotropy (Morales et al. 2014).

As $MgSiO_3$ post-perovskite cannot be recovered to ambient conditions, direct exploration of its properties is restricted to *in-situ* diamond cell experiments where deformation is limited to low-strain axial compression. Using X-ray diffraction, Miyagi et al. (2010) showed that under these conditions $MgSiO_3$ post-perovskite generates textures consistent with dominant slip on (001). Under similar conditions the $MnGeO_3$ analogue seems to deform by the same mechanism (Hirose et al. 2010). Earlier results from similar experiments undertaken by Merkel et al. (2006, 2007), which suggested slip on (100), are probably better explained as a transformation texture (see Walte et al. 2009, Miyagi et al. 2011, Okada et al. 2010). Lower pressure analogues can be deformed, in large volume deformation apparatus (e.g. the D-DIA, Durham et al. 2002, Wang et al. 2003), to significant strain at high pressure and temperature. These analogues can also be recovered and subject to direct analysis. The best known and most studied of the low-pressure $MgSiO_3$ post-perovskite analogues is $CaIrO_3$. Its dominant dislocation slip system has been inferred by electron back-scatter diffraction (EBSD) and transmission electron microscope (TEM) analysis of recovered samples (Yamazaki et al. 2006, Walte et al. 2007, Miyajima and Walte 2009), and from *in-situ* X-ray diffraction (Miyagi et al. 2008), to be [100](010). The same slip system was observed to be active during deformation of $CaPtO_3$ (McCormack et al. 2011). These and other analogues (Dobson et al. 2011) can provide critical experimental constraints on the likely viscosity (Hunt et al. 2009, Dobson et al. 2012), thermal conductivity (Hunt et al. 2012), and phase transition mechanism (Dobson et al. 2013), of post-perovskite in the lowermost mantle.

A large number of atomic-scale simulations of the elementary processes that contribute to

deformation of post-perovskite complement the experiments. Notably, Ammann et al. (2010) simulated deformation via point-defect diffusion while Carrez et al. (2007a,b) investigated deformation via the glide of dislocations. This motion is simulated via the Peierls–Nabarro model of a dislocation (Peierls 1940, Nabarro 1947) with the non-elastic interactions derived from electronic structure calculation of the energy of generalised stacking faults (see Carrez and Cordier 2010, Walker et al. 2010). Metsue et al. (2009) used the same approach to determine the stress needed to move various dislocations in $CaIrO_3$ and $MgGeO_3$ post-perovskite, compared these with $MgSiO_3$, and used visco-plastic self-consistent (VPSC) modelling to simulate the generation of CPO in simple shear. Their results suggest that the weakest slip system, thus CPO pattern, varies with chemistry with [001](010), [100](001) and [001](010) dominating for $MgSiO_3$, $MgGeO_3$ and $CaIrO_3$, respectively. They predict median CRSS of the secondary slip systems to be ~ 4 times that of the primary one in $MgSiO_3$ and $MgGeO_3$ and in $CaIrO_3$ the ratio of the CRSS for the two weakest slip systems is 1 : 7.5, although they do not predict the correct primary slip system.

Despite many studies investigating the deformation properties of post-perovskite, its CRSS ratios and plastic anisotropy have not been constrained by experiment. To address this, we have combined *in situ* measurements of CPO development during simple shear of $CaIrO_3$ post-perovskite with VPSC modelling to determine the CRSS ratio and degree of plastic anisotropy appropriate for simulation of CPO generation in the lowermost mantle.

2 Method

Post-perovskite $CaIrO_3$ was deformed in simple shear using the D-DIA (Durham et al. 2002, Wang et al. 2003) on beam-line X17B2 at the National Synchrotron Light Source, Brookhaven National Laboratory. During deformation X-ray diffraction data were collected, using the 10-element energy dispersive detector described by Weidner et al. (2010), and analysed for the evolution of stress and texture with applied strain. The detector is optimised for the measurement of stress on a sample from elastic deformation of the sample and the resulting change in the energy of the Bragg peaks as a function of the detector position. Measurement of sample texture (i.e. the distribution of orientations of the grains in the sample) using this detector is possible but more challenging as it requires robust measurement of each peak's intensity as a function of detector position which, as described below, is influenced by factors external to the sample. Nevertheless, we have calculated the CPO as a function of strain from the sample using the method described below. The sample was recovered and subject to scanning electron microscope (SEM) analysis to better quantify the texture and determine further details of the sample microstructure. To relate the texture development to the properties of $CaIrO_3$ post-perovskite, we undertook VPSC modelling, using a range of values for the different slip systems CRSSs, and compared the models to the X-ray derived textures.

2.1 Experiment details

The $CaIrO_3$ sample was synthesised at 3 GPa and 1350 °C for 20 hours from the same batch of CaO and IrO_2 used previously by Hunt et al. (2009, 2012). Laboratory X-ray diffraction measurements of the sample showed complete reaction with a small amount (~2 vol. %) of residual IrO_2. The excess IrO_2 prevents the growth of Ca-rich oxides such as Ca_2IrO_4 (Lindsay-Scott et al. 2007).

The 1.5 mm diameter presynthesised block was cut into a 0.5 mm thick slice at 45° to the cylinder axis. This was sandwiched between two corundum pistons, which had the ends contacting the sample cut at 45°, in the simple-shear geometry. These were surrounded by a sleeve

of MgO, a 2.4 mm diameter, 50 µm thick, inconel furnace, a sleeve of crushable Al_2O_3 and the pressure medium, which was a 6 mm cube of baked pyrophyllite. A D-type thermocouple ($W_{97}Re_3/W_{74}Re_{26}$) was inserted into the assembly such that it butted against, but was insulated from, the furnace. The sample was oriented such that the normal to the 45° sample faces was perpendicular to the X-ray beam. The thermocouple was also perpendicular to the beam. The sample geometry is illustrated in Figure 1.

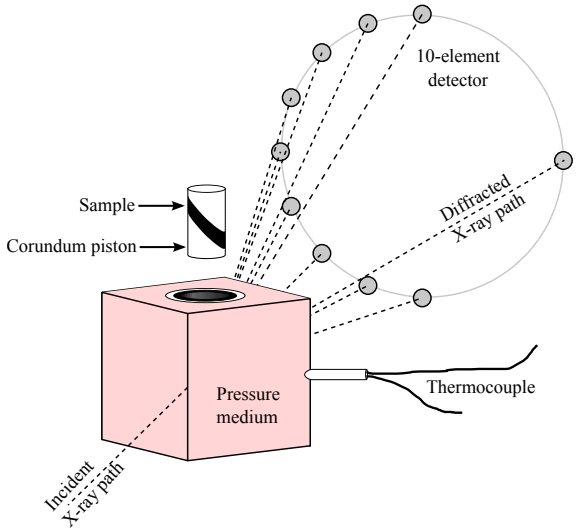

Figure 1: Illustration of the sample assembly and elements of the 10-element detector. The detectors are positioned at $2\theta = 6.5°$ and $\psi = 0$, 90, 180, 202.5, 225, 247.5, 270, 292.5, 315 and 337.5° clockwise when observed along the X-ray beam. For clarity the sleeve and end caps which surround the sample are omitted.

The assembly was compressed in the D-DIA to around 3 GPa using 4 sintered diamond and two tungsten carbide anvils, all with 4 mm truncations. The sample was heated to 400 °C and annealed for 20 minutes before deformation was started.

During deformation the differential pistons were advanced at at rate of ~ 5 µm min^{-1} and diffraction patterns were collected continuously with 120 s exposure times. The incident X-ray beam was 100 × 100 µm and the diffracted beams were around 10 µm high (Weidner et al. 2010). Deformation of the sample was observed using X-radiography with images recorded before and after deformation. No images were recorded during deformation. After 70 minutes, the experiment was quenched, deformation stopped and decompressed. The sample was recovered for SEM analysis.

2.2 Radiographic image analysis: total strain and sample orientation

Radiographic images from before and after deformation were used to determine the total strain imparted to the sample. $CaIrO_3$ is opaque to synchrotron X-rays and therefore the metal foil strain-markers often used in simple shear experiments (e.g. Ohuchi et al. 2010) could not be used as they would be obscured by the sample. However, the edges of the opaque sample are clear in the X-radiographs and these are used to determine the shear strain and orientation of the sample during deformation. Parallelograms were fitted around the edges of the sample, from which the thickness (l), acute inter-edge angle (η), and the orientation, represented by the angle the long edge of the parallelogram makes with the horizontal (χ), was measured (Figure 2). η was measured at both ends of the sample and averaged. The shear strain (γ) was calculated

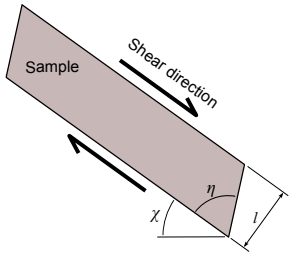

Figure 2: Cartoon of the distances and angles measured in the sample and used to calculate strain. The grey rectangle is the sample and the black arrows show the shear direction.

from:

$$\gamma = \frac{l_e \tan \eta_e - l_b \tan \eta_b}{\bar{l}}, \tag{1}$$

where $\bar{l}$ is the mean thickness of the sample and subscripts b and e denote the measurements before and at the end of deformation. Change in the sample thickness during deformation implies that deformation deviates from simple shear and use of the mean thickness is a simple way of removing the effect of sample thickness from the strain analysis. Furthermore, the corundum pistons used in the experiment were too short to prevent rotation of the of the sample during deformation. The angle that the major axis of the parallelogram makes with the horizontal is thus used to define the orientations of the shear plane during deformation and relevant directions to plot textural data.

2.3 X-ray Diffraction Data and Analysis

The 10-elements of the diffraction detector were calibrated for energy using Co-57 radioactive decay energies and for D-spacing and intensity using a corundum standard prior to the experiment. Eight of the elements were used in the current experiment: the detector at $\psi = 292.5°$ was broken whilst semi-automatic peak fitting software used is unable to process the data from the element at $\psi = 90°$.

The diffraction peaks usable in the texture calculation are limited to those with sufficient intensity to be readily identifiable, are present in the vast majority of the diffraction patterns, and do not overlap with Pb or Ir fluorescences. Five $CaIrO_3$ diffraction peaks, listed in Table 1 and highlighted in the example diffraction pattern in Figure 3, met these criteria. The intensity and d-spacing of the peaks was obtained by fitting the data with a Gaussian-Lorentzian peak on top a linear background, using the Plot85 software package[1]. Fitting the peaks individually, resulted in significant background variation between temporally adjacent patterns leading to large fluctuations in the fitted peak intensities. To minimise this, the peaks were fit in the groups listed in Table 1, and within each group the peaks were constrained to have the same Full Width at Half Maximum. In some patterns it was necessary to include one or two additional peaks corresponding to diffraction peaks from the MgO sleeve or inconel furnace. Despite fitting the peaks in groups, the diffraction data are sufficiently noisy that, in the following analysis, it was necessary to smooth the data with a moving average over three diffraction patterns. Additionally, some of the measured peaks intensities deviated significantly from the other measurements of the same peak in the same detector; these observations were discarded. One whole set of diffraction patterns at $\gamma = 0.694$ were discarded because the majority of the diffraction intensities differed significantly from those measured at other similar strains.

[1]Plot 85 is available from http://www.mpi.stonybrook.edu/NSLS/X17B2/Software/software.htm

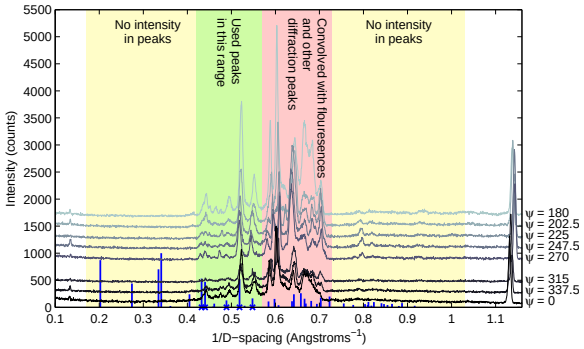

Figure 3: Example diffraction patterns from the detector at $\gamma = 0.289$ as a function of ψ. The gap in the data between $\psi = 270°$ and $\psi = 335°$ is because the detector at 292.5° was not functioning. The vertical lines denote the zero pressure $CaIrO_3$ diffraction peak positions and relative intensity in a powder pattern. The green highlighted area is the range within which the usable diffraction peaks are located and the five peaks highlighted with crosses are those used in the analysis (Table 1). The peaks at $1/D \approx 0.13$ and $1.14 Å^{-1}$ are the Co-57 gamma ray peaks used to calibrate the detector elements.

Peak *hkl*	Intensity in powder pattern (%)	Fitting group and number of extra peaks	Mean intensity in reference patterns (arbitrary units)*
(112)	53.1	} 0	53.1
(130)	47.0		69.4
(042)	12.7	} 1-2	72.6
(132)	51.9		545.1
(004)	16.4		231.4

Table 1: Fitted peaks and peak groupings. The intensities of a powder pattern are taken from Martin et al. (2007). *The mean measured intensities are the mean of the data from the first three diffraction patterns, from all of the detectors. The reported values are scaled such that the intensity in the (112) peak is the same as that in a powder pattern.

Pressure and differential stress in the sample were calculated from the displacement of the diffraction peaks, using the elastic strain model of Singh et al. (1998). The single crystal elastic constants and thermal expansion used were from Stølen and Trønnes (2007) and Lindsay-Scott et al. (2007) respectively.

The texture in the sample is determined from the variation in the intensity of the diffraction peaks around the Debye-Scherrer rings as observed in each of the detectors. The measured intensities of the peaks are strongly dependant on X-ray wavelength (Table 1) and, without a normalisation of the intensities, the method detailed below gives an apparent texture which is physically meaningless. Consequently, we normalise the intensities prior to computing the texture under the assumption that the crystal orientations are uniform prior to deformation. This process involves an independent normalisation factor for each *hkl* in each detector. The normalised intensity, I', is calculated from:

$$I'_{hkl,\psi,t} = I_{hkl,\psi,t} \times \frac{c_{hkl}}{I_{hkl,\psi,ref}} \tag{2}$$

where I is the measured intensity at time t and detector position ψ, and c is the intensity expected for each *hkl* peak in a powder diffraction pattern. The c_{hkl} values used were those of

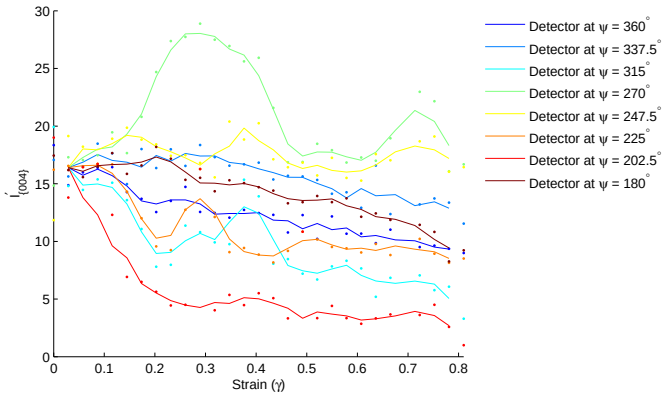

(a)

Figure 4: Normalised intensities (I') of the {004} peak plotted against strain for each detector. The dots are the data and the lines the moving average from which the ODFs are calculated.

Martin et al. (2007), at 1 bar, 293 K, as reported in the American Mineralogist Crystal Structure Database (Downs and Hall-Wallace 2003). We note that using c_{hkl} values from other studies reporting a $CaIrO_3$ powder pattern (e.g. McDaniel and Schneider 1972, Rodi and Babel 1965) makes negligible difference to the analysis. An alternative approach to peak normalisation, adding the change in intensity ($\Delta I = I_{hkl,\psi,t} - I_{hkl,\psi,ref}$) to the intensities in a powder pattern was considered. However, because additional scale factors are required this approach was not used.

The normalised intensities (I') for the (004) peak are plotted in Figure 4. The normalisation forces all the detectors to have the same value of I' at the beginning of the experiment, from which point the intensities diverge as texture develops in the sample. There is a general decrease of intensity with strain is a feature of all the diffraction peaks and a consequence of the expected reduction in intensity of the X-ray source with time. The relatively large medium term increases and decreases in intensity (e.g. between $\gamma = 0.2$ and 0.4 in detector at 270°, Figure 4) are caused by changes to the population of grains in the diffraction condition.

As a consequence of the limited number of usable diffraction peaks, our data is relatively insensitive to the (100) crystallographic direction It only provides limited coverage of $(2\theta, \psi)$ space, plotting as 8 discreet points at $[(180-2\theta)/2, \psi]$ in a pole figure. We therefore inverted the peak intensities (I') for an orientation distribution function (ODF) using the method described by Hielscher and Schaeben (2008) and implemented in version 4.0.20 of the MTEX toolbox (Bachmann et al. 2010). The inversion made use of a 'de la Vallee-Poussin' kernel with a 13° half-width. The ODF, $f(g)$:

$$\frac{\Delta V(g)}{V} = f(g)\mathrm{d}g \tag{3}$$

is a continuous function describing the volume fraction of crystals, $\Delta V(g)$, with Euler angles $g(\varphi_1, \Phi, \varphi_2)$. Where $\mathrm{d}g$ is an infinitesimal volume element, and V is the total volume of the sample (see Mainprice et al. 2014). For a uniform distribution of crystal orientations, $f(g) = 1$. Along with the crystal structure and structure factors, an orientation distribution function can be used to predict the intensity of the diffraction peak arising from a particular lattice plane for each detector position. To track the development of CPO with strain in the experiment we plot inverse pole figures for orientations parallel to the shear direction $[\chi, 90]$ and normal to the shear plane $[\chi + 90, 90]$ from the calculated ODFs.

2.4 SEM analysis

The recovered sample was mounted and polished to enable SEM analysis. The final polish was a chemical polish using 0.03 µm colloidal silica in an alkaline solution. The sample was then coated with a thin carbon layer and analysed using electron back-scattered diffraction (EBSD) in the X500 CrystalProbe field emission gun (FEG) SEM at the University of Liverpool. Electron back-scatter diffraction patterns (EBSPs) were obtained over a 115×95 µm area with 0.5 µm grid spacing. The accelerating voltage was 20 kV, the beam current 35 nA and the working distance 25 mm. EBSPs were automatically indexed using the Oxford Instrument's HKL CHANNEL 5 software package and the single crystal structure of Martin et al. (2007).

Measured crystal orientations from the EBSD were used to create an ODF representing the final texture in the sample. Each grid point where a EBSP was successfully indexed was assigned an equal volume weighting and these orientations were used to fit an ODF using MTEX. This ODF was then used for comparison with the X-ray derived texture. Larger grains in the EBSD, therefore have more weighting in the ODF, similar to the X-ray data in which larger grains will contribute more to the diffraction pattern than smaller grains.

2.5 VPSC modelling

The relative activity of the less active slip systems during deformation of $CaIrO_3$ was investigated using VPSC modelling. We ran a number of models with a range of CRSS values generated by modification to the models used by Metsue et al. (2009) and Miyagi et al. (2008) and compared the output of these models to the X-ray derived texture data. In our calculations, and in common with the majority of previous work on post-perovskite, we make use of the Tangent linearisation scheme (Lebensohn and Tomé 1993) as implemented in version 7c of the Los Alamos VPSC code (Molinari et al. 1987, Lebensohn and Tomé 1993, Lebensohn et al. 2007). The strain rate accommodated by each slip system, s, is assumed to follow a power law:

$$\dot{\gamma^s} \propto \left(\frac{\tau_r^s}{\tau_0^s} \right)^n, \tag{4}$$

where the strain rate, $\dot{\gamma^s}$, is determined by the ratio of the shear stress resolved onto the slip plan acting in the direction of the Burgers vector, τ_r^s to some slip system dependent critical resolved shear stress, τ_0^s, which is a parameter of the calculation. For the majority of our models we assume constant value for the power law exponent $n = 3$, but to test the effect of the stress exponent ran a complementary series of models with $n = 2$ and $n = 5$.

The calculations were started with a sample of 2000 grains drawn randomly from a uniform orientation distribution. This model polycrystal is then subject to 50 equal strain increments in simple shear leading to an overall shear strain of 0.81 at the end of the calculation with the orientation of each grain stored at the end of each strain increment. In order to compare the calculations with the experimental results derived from the X-ray data we model the effect of the detector geometry using the same method as that used for the EBSD data, detailed below.

2.6 Comparison and analysis of ODFs

Before we can compare the texture derived from X-ray diffraction, EBSD and VPSC modelling we need to account for the limitations imposed by the X-ray diffraction system and the lack of observations of diffraction from planes nearly parallel to (100). To do this, we fit ODFs to the EBSD measurements and the VPSC simulations, from which the intensity of the diffraction peaks, present in the X-ray data (Table 1), are estimated at the position of the active detectors. These intensities are then re-inverted using the same approach as that used for the X-ray data,

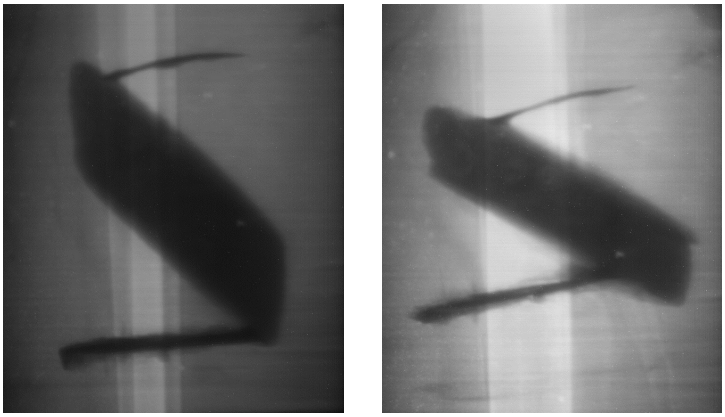

Figure 5: Radiographic images from before (left) and after (right) the sample was deformed. The sample is the large dark parallelepiped. The relatively light vertical stripe is the gap between the sintered diamond anvils.

allowing the different data sets to be compared on an equal footing. In particular, this approach of simulating the X-ray diffraction experiment allows the strength of the texture to be compared.

Alongside the maximum and minimum values of the inverse pole figures, we use the Texture Index as a simple measure of texture strength. It is calculated directly from the ODF:

$$J_{\mathrm{ODF}} = \int |f(g)|^2 \mathrm{d}g. \tag{5}$$

The absolute value of J increases as $f(g)$ becomes less uniform and the texture increases in "strength", indeed J is 1 for a uniform distribution and infinity if the ODF contains a single crystal orientation. Integrating $f(g)^2$ means that the value of J_{ODF} is dominated by orientations where $f(g)$ is large.

3 Results

Analysis of the X-radiographs from the start and end of the experiment shown in Figure 5 using Equation 1 gives $\gamma = 0.90$ for the left hand end of the sample and $\gamma = 0.72$ at the right hand end. The mean total strain in the sample is 0.81 ± 0.13 and the mean shear strain-rate was $2.33 \pm 0.37 \times 10^{-4}\,\mathrm{s}^{-1}$. The long axis of the sample during deformation rotated from $\chi = 312°$ to 298°. The pressure during the experiment was 3.2 GPa, the temperature constant at 400 °C and the differential stresses increased with strain from around 0.5 to 1.4 GPa. In the following analysis the rotation- and shear strain-rate of the sample are both assumed to be constant during deformation.

Inverse pole figures from the EBSD analysis of the recovered sample (Figure 6a) show that poles to the (010) plane preferentially align normal to the shear plane while the (100) direction aligns in the shear direction. This is the same deformation texture that has been observed previously for $CaIrO_3$ deformed in simple shear and suggests deformation is permitted by the motion of dislocations with [100] Burgers vectors gliding on (010) (e.g. Walte et al. 2007, Yamazaki et al. 2006). The strength of the texture measured here is very similar to that reported by Walte et al. (2007) in their simple shear experiment to the same total strain. The temperature in their experiment was 1000 °C rather than the 400 °C in our experiment. Suggesting that temperature does not have a significant effect on texture development in $CaIrO_3$. In addition to this textural information, the SEM analysis allows us to measure the grain size and shape. We find that the modal grain-size of the sample is between 2 and 5 µm and that the shapes of

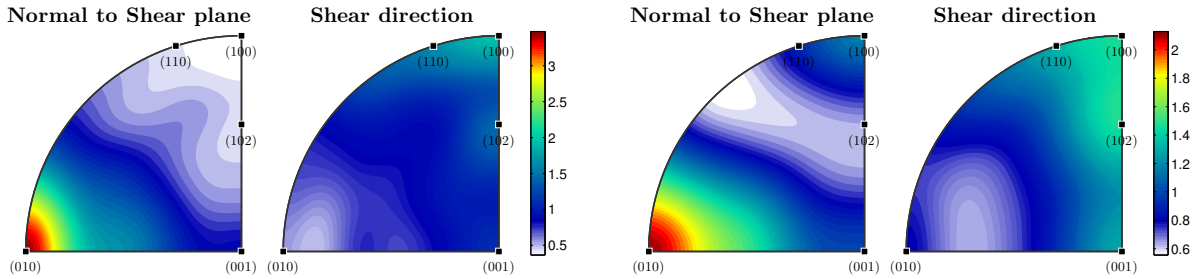

(a) Raw EBSD **(b)** Modelled EBSD

Figure 6: Inverse pole figures of EBSD data. (a) The measured (raw) data and (b) the inverse pole figures after simulating the effect of the 10-element detector. Left inverse pole figure shows poles normal to the shear plane and right is in the shear direction. The scale is multiples of a random distribution. Note the difference in scale between the two figures.

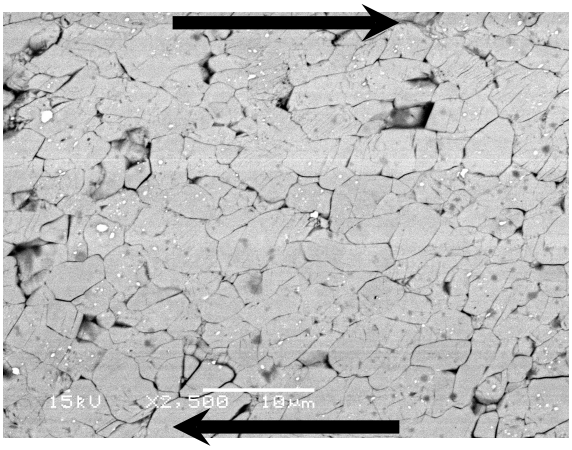

Figure 7: Back-scatter electron image of deformed sample. The shear direction is shown by the overlaying arrows.

the grains are close to equant (Figure 7). Grains with an identifiable long axis do not show a strong shape preferred orientation.

Modelling the effect of the detector and the 5 diffraction peaks on the ODF gives the modelled textures shown in Figure 6b. The location of the maximum normal to the shear plane is not altered by the combination of detector geometry and peak selection, although the maxima is reduced in magnitude. However, the shear direction maximum becomes broader and its location moves to be close to the (102) direction, again with a reduced magnitude. The change in texture is a consequence of the particular set of diffraction peaks used and the position of the detector elements. Specifically, the peaks present in the X-ray data are at a high angle to (100), so crystals oriented with this plane in the diffracting condition are not as well represented in the recovered texture. The reduction in the range of intensities in the modelled EBSD inverse pole figures is a consequence of both the number of peaks in the X-ray data and the sparsity of coverage in the pole figures. Indeed, modelling the EBSD data using the first 25 strong ($> 10\,\%$) peaks of the $CaIrO_3$ diffraction pattern recovers the same texture as is observed in the raw EBSD but with a reduced intensity range.

The texture as a function of strain recovered from analysis of the X-ray data is shown as inverse pole figures with a common intensity scale in Figure 8. A non-uniform texture develops and strengthens with increasing strain and, for the most part, this is represented by the development of intensity of the (010) component normal to the shear plane. This observation

is consistent with the glide plane observed in previous studies of deformation of $CaIrO_3$ (e.g. Walte et al. 2007, Yamazaki et al. 2006). However, the maximum intensity in the shear direction is close to (102). The texture is consistent with that of the modelled EBSD data's apparent texture (Figure 6b) and strongly suggests that this texture is an anomaly introduced by the detector geometry and peak selection. The variability in maxima locations is caused by short term variations in the X-ray peak intensity as the population of grains in the diffraction condition changes (*e.g.* Figure 4).

The increase in maximum and decrease in the minimum value in the pole figures as a function of strain is summarised by Figure 9. The data are consistent with a strengthening texture in the sample. In the shear direction (Figure 9b), the range of values extracted from X-ray data at the end of the experiment are marginally greater than those found from the EBSD analysis. Normal to the shear plane (Figure 9a), though the maximum values in the X-ray data are less than those of the modelled EBSD.

An alternative approach to evaluating the evolution of the strength of the texture with increasing strain is to evaluate the texture index of the underlying ODF as shown in Figure 10. The development of texture is clear from the increase in texture index with strain. As the texture index is an integral over the whole of the ODF (Equation 5) and the indices do not relate to the location of the maxima and minima of the ODF but only to its strength, it is a useful tool in comparing the rate of texture development from the analysis of X-ray data, the EBSD measurements, and the VPSC modelling. As shown in Figure 10, analysis of the X-ray data predicts a stronger texture index than is indicated by our modelling effect of the detector geometry and peak selection given the EBSD results. However, Monte-Carlo modelling indicates that even in the absence of any other sources of error, the X-ray data is expected to overestimate the texture index merely from the statistical errors in the X-ray peak intensities. Errors in the X-ray data adds noise to the ODF and this inevitably increases the texture index.

There are a number of other sources of error that may explain the discrepancies between the X-ray and the modelled EBSD data. The comparison of the EBSD and X-ray data sets assumes that there was no texture in the sample before deformation, a hypothesis that is not directly testable. It also assumes that the EBSD measured CPO is the true texture in the sample. EBSD and X-ray diffraction probe different sections of the sample and, at least, in steel more than 10^4 grains need to be indexed (not 10^4 orientation measurements) to properly match the textures measured by the two methods (Wright et al. 2007). As already discussed the noise in the diffraction patterns required that a moving average was used when calculating the CPO. However, the principle sources of error in the experiment are the measured intensities in the diffraction patterns. In particular, the anvil gap increases during deformation and the sample rotates (Figure 5). This behaviour changes the path length of the diffracted X-ray beam through the sample and anvils for each detector during the experiment and hence alters the relative sizes of the measured diffraction peaks. This leads to variation in the background above which the peaks are fitted and requires that the peak shape and intensity during deformation must be allowed to alter alongside the relative weighting of the background in the peak fitting routine. It is notable that most of this change takes place in the detectors at 202.5 and 337.5° (Figure 4) and that the detectors at 0 and 180° maintain a view through the anvil gap for the whole experiment. The change in the experimental geometry during deformation leads to variations in the measured intensity of the X-ray peaks with strain and hence to artefacts in the calculated CPO. Correcting for this phenomenon would require diffraction from an undeforming reference material alongside diffraction from the sample. We did not collect diffraction from the undeforming corundum pistons and so cannot make such a correction. In developing the analysis method, a number of additional steps and alternative approaches were trailed to determine if they mitigated these sources of error and improved the correspondence between the EBSD and

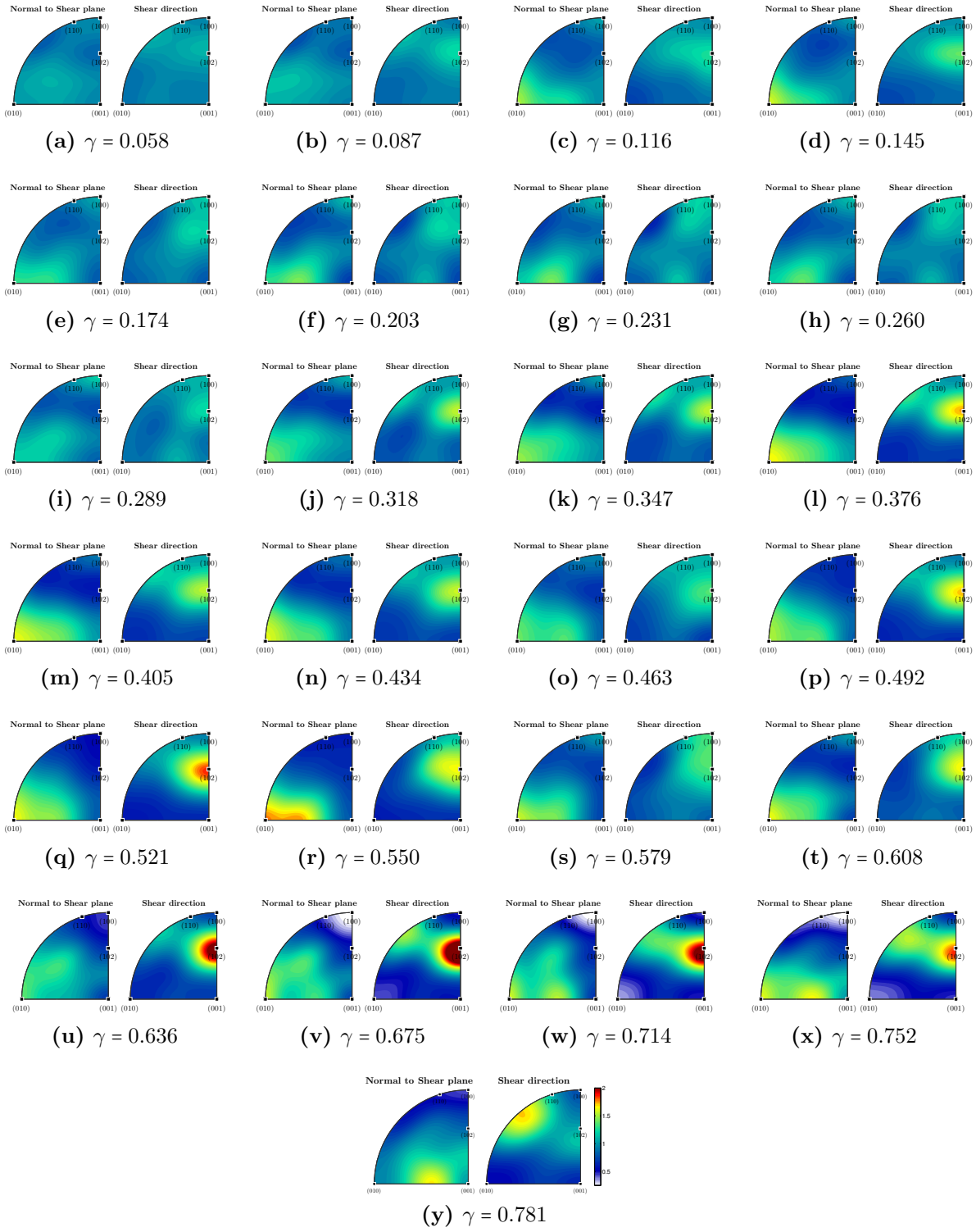

(a) $\gamma = 0.058$ **(b)** $\gamma = 0.087$ **(c)** $\gamma = 0.116$ **(d)** $\gamma = 0.145$

(e) $\gamma = 0.174$ **(f)** $\gamma = 0.203$ **(g)** $\gamma = 0.231$ **(h)** $\gamma = 0.260$

(i) $\gamma = 0.289$ **(j)** $\gamma = 0.318$ **(k)** $\gamma = 0.347$ **(l)** $\gamma = 0.376$

(m) $\gamma = 0.405$ **(n)** $\gamma = 0.434$ **(o)** $\gamma = 0.463$ **(p)** $\gamma = 0.492$

(q) $\gamma = 0.521$ **(r)** $\gamma = 0.550$ **(s)** $\gamma = 0.579$ **(t)** $\gamma = 0.608$

(u) $\gamma = 0.636$ **(v)** $\gamma = 0.675$ **(w)** $\gamma = 0.714$ **(x)** $\gamma = 0.752$

(y) $\gamma = 0.781$

Figure 8: Inverse pole figures with strain during our experiment. Left inverse pole figure shows poles normal to the shear plane (glide plane) and right is in the shear (glide) direction. All the pole figures are plotted on the same colour scale as y.

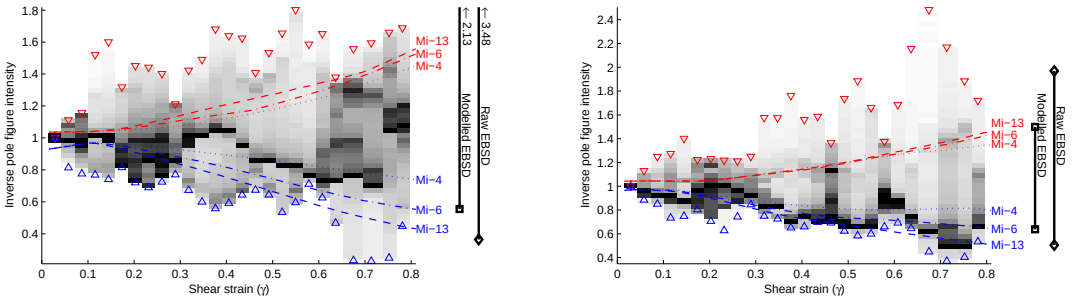

(a) Normal to shear plane **(b)** Shear direction

Figure 9: Histograms of the inverse pole figure intensities recovered from X-ray data. The grey histograms are normalised intenstity disribution from each inverse pole figure; the maximum ($\triangledown$) and the minimum ($\triangle$) values are highlighted. The black bars at the right of the figures are the measured and modelled intensity ranges of the EBSD data (Figure 6). The dashed, dash-dot and dotted lines are the maximum and minimum values in the equivalent inverse pole figures from the corresponding VPSC models, after modelling the effect of X-ray detector (see text for details).

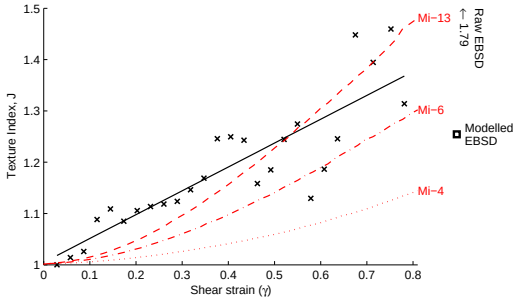

Figure 10: Texture Index (black crosses) as a function of strain. The solid black line is robust best fit line to data. The red lines are a selection of the VPSC models which bracket the observed experimental values. The black square is the modelled EBSD value. The raw EBSD's texture index (J = 1.79) is off the scale of the figure.

the X-ray data. In addition to alternative approaches to the intensity normalisation, which are described above (section 2.3), we tested five other possible procedures: (a) interpolation of data between detector points (e.g. Bollinger et al. 2012); (b) replicating and rotating the data 180° (using the symmetry of the deformation experiment); (c) smoothing the ODF; (d) subtracting a reference ODF from each ODF in the series to force the ODF at zero strain to be uniform; and (e) using additional, less well constrained, diffraction peaks in the analysis. These tests were not found to be beneficial to the analysis and so were not utilised.

3.1 VPSC models

The measurement of texture as a function of strain in this study provides a useful data set with which to explore the performance of models of the deformation of $CaIrO_3$ post-perovskite. One key aspect of these is the relative CRSS (or τ_0) of the less mobile slip systems. We have run a series of VPSC models based on two models from the literature. The first is based on Peierls-Nabarro modelling (Metsue et al. 2009), where the CRSS was assumed to be proportional to the

Peierls stress for each slip system. The second is an empirical model used by Miyagi et al. (2008) to determine the active slip systems in a sample deformed in axial compression. In each of our models the values of the CRSS for slip systems other than the weakest one were scaled in order to explore how changing the plastic anisotropy altered the rate of texture development and in two models the stress exponent was also changed. Scale factors were between 0.5 (increasing the plastic anisotropy) and 12 (making the model less anisotropic) and stress exponents between $n = 2$ and 5. The CRSS values for all models are listed in Table 2. VPSC models were run to simulate the development of texture in simple shear (to $\gamma = 0.81$). The inverse pole figures as a function of strain for each of the models are shown in the Supplementary Information Figures.[2] To compare the VPSC models with the X-ray data, simulated X-ray peak intensities at the detector positions were calculated from ODFs fitted to the VPSC data.

The VPSC models based on the results of Metsue et al. (2009, Met-N, Figure 11a, Supplementary Information Figure S1) are dominated by slip on the (001) plane and all give a qualitatively different texture to that observed in the EBSD data (Table 2). Modelling the effect of the X-ray diffraction geometry (Figure 11b) did not alter the texture to match that recovered from the X-ray data. Changing the strength (τ_0) of the secondary slip systems affected the rate of CPO development but did not significantly change the character of the texture. On the other hand, models derived from the empirical parametrisation of Miyagi et al. (2008, Mi-N, Figures 11c and e and Supplementary Information Figure S2) give a CPO that is similar to the EBSD result, with the maximum normal to the shear plane close to the pole to (010) and (100) in the shear direction. In the lower N models ($N \leq 13$), the maximum in the inverse pole figure normal to the glide plane has a tight distribution around the (010) direction, while in the higher N models the maxima moves towards (100) as the secondary slip systems strengthen. Increasing the stress exponent, n, at constant CRSS values (Mi-N-nn models: Table 2 and Supplementary Information Figure S3) has a similar effect to increasing the strength of the secondary slip systems. It results in stronger textures and a change in position of the maxima in the inverse pole figures. Modelling the effect of the 10-element detector on the Mi-N VPSC textures has a similar effect to that on the EBSD data, namely moving the apparent glide direction from (100) to around (102) (Figures 11d and f). We emphasise here that the X-ray diffraction geometry only imparts an apparent texture to some CPOs. For example, both the modelled and unmodelled Met-31 have almost the same texture (Figures 11a and b) and only minor changes in intensities of the inverse pole figures.

In all the Mi-N models, the range of intensities present in the modelled inverse pole figures at $\gamma = 0.81$ were less than the values in the X-ray data (Figure 9) but are comparable with the modelled EBSD intensities. The VPSC models develop an inital CPO aligned $\sim 30^\circ$ from the shear direction, which rotates into the ideal geometry above $\gamma \sim 0.2$. The rate of rotation is inversely proportional to the strength of the secondary CRSSs and none of the VPSC models reach the ideal geometry by $\gamma = 0.81$.

A constraint of the relative strength (or CRSS) of the secondary slip systems is provided by comparing the texture development (the maximum, minimum and range of intensities in the pole figures and the texture index) in the X-ray data and the VPSC models. For the experiment here, the best matches for the inverse pole figure intensity and texture index between VSPC models and the EBSD analysis, at $\gamma = 0.81$, is for the Mi-25, Mi-13 and Mi-6 models, with Mi-13 being marginally superior. The models all compare well in some regards and poorly in others, which highlights the deficiencies of using a single value for the activities of the secondary slip systems and the limitations of the VPSC model. The limitations of the VPSC model are seen in the functional form of the texture index values; below $\gamma \sim 0.4$ they are approximately

[2]The Supplementary Information for this manuscript contains only the inverse pole figures of the VPSC models.

VPSC Model		Met-62	Met-31	Met-16	Mi-50	Mi-25	Mi-13	Mi-6	Mi-4	Mi-13-n2	Mi-13-n5
scale factor		0.5	1	2	1	2	4	8	12	4	4
stress exponent (n)		3	3	3	3	3	3	3	3	2	5
Slip system		CRSS values									
[100](010)		23.2	11.6	5.8	1	1	1	1	1	1	1
[100](001)		62.2	31.1	15.55	50	25	12.5	6.25	4.167	12.5	12.5
[100]{011}		136.8	68.4	34.2	50	25	12.5	6.25	4.167	12.5	12.5
[001](010)		1	1	1	50	25	12.5	6.25	4.167	12.5	12.5
[001]{110}		78.6	39.3	19.65							
[001](100)		117.8	58.9	29.45	50	25	12.5	6.25	4.167	12.5	12.5
[010](100)		24.2	12.1	6.05	50	25	12.5	6.25	4.167	12.5	12.5
[010](001)		15	7.5	3.75	50	25	12.5	6.25	4.167	12.5	12.5
⟨110⟩(001)		38.4	19.2	9.6							
⟨110⟩{110}		84	42	21	50	25	12.5	6.25	4.167	12.5	12.5
⟨101⟩(010)					50	25	12.5	6.25	4.167	12.5	12.5
⟨101⟩{111}					100	50	25	12.5	8.333	25	25
Properties at $\gamma = 0.81$											EBSD
CPO		[290](001)	[150](001)	[150](001)	[950](190)	[920](190)	[100](010)	[100](010)	[100](010)	[100](010)	[981](190)	[100](010)
Normal to	max	4.68	2.80	2.40	2.28	2.26	2.31	2.40	2.36	1.52	2.38	3.48
shear plane	min	0.03	0.07	0.09	0.18	0.22	0.29	0.48	0.62	0.48	0.14	0.36
Shear direction	max	3.61	2.97	2.67	1.99	2.04	2.10	2.13	2.00	1.42	2.13	1.96
	min	0.01	0.07	0.07	0.08	0.11	0.16	0.34	0.64	0.56	0.08	0.50
Texture Index		2.53	1.84	1.67	2.18	2.06	1.87	1.60	1.32	1.65	2.31	1.79
S-anisotropy ($\ln(\xi)$ %)		4.53	0.39	0.41	3.03	2.88	2.52	1.80	0.61	2.12	3.10	2.61
P-anisotropy ($\ln(\phi)$ %)		5.39	3.62	3.26	−4.15	−3.98	−3.66	−2.99	−1.78	−3.32	−4.24	−4.30

Table 2: CRSS values of the VPSC models and their properties at $\gamma = 0.81$. The models Met-N are based on the CRSS values of Metsue et al. (2009) and the Mi-N models are based on Miyagi et al. (2008). The Mi-N-nn models have the stress exponent changed. The number N in each model median secondary slip system CRSS in the model; the Met-31 and Mi-50 models are the same as those used in the previous studies. The properties of the VPSC models are for the output of VPSC model without applying the effect of the 10-element detector. The same values from the EBSD data are shown for comparison. The CPO directions reported are the hkl closest to the actual position of the maximum in the inverse pole figure with single digit ordinals (i.e. (971) is possible but (10,11,13) is not). The greatest directional error is therefore for directions with 9 as one of the hkl values.

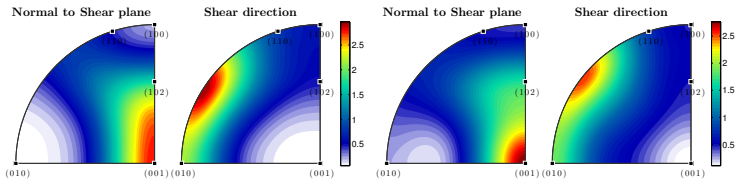

(a) Met-31 **(b)** Met-31, modelled

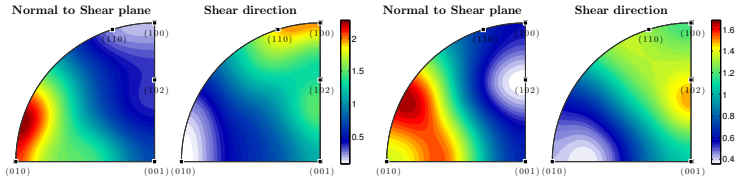

(c) Mi-50 **(d)** Mi-50, modelled

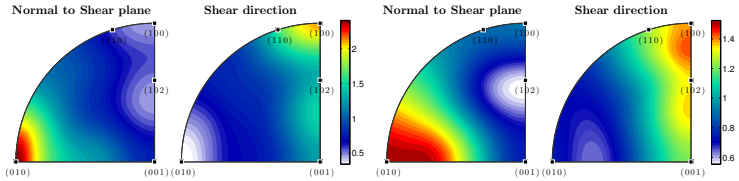

(e) Mi-6 **(f)** Mi-6, modelled

Figure 11: Inverse pole figures at $\gamma = 0.81$ for the VPSC models indicated, both before and after simulating the effect of the 10-element detector. Left inverse pole figure shows poles normal to the shear plane (glide plane) and right is in the shear (glide) direction. Note the difference in scale between the different figures.

parabolic and thereafter the values increase more or less linearly. This is in contrast to the Texture Index values from the X-ray data which increase in an approximately linear manner for all γ. Decreasing the difference between the CRSSs or reducing the stress exponent in the VPSC models reduces the rate at which the texture index develops (Figure 10). The VPSC model that best matches the rate of texture index increase in the X-ray data as well as the EBSD data is Mi-4 which has secondary CRSS values 4.17 times that of the primary [100](010) slip system. The secondary slip systems in $CaIrO_3$ are therefore between 12.5 (model Mi-13) and 4.17 (Mi-4) times stronger than the primary slip system. Compromising between the two models, the best value for the secondary slip-systems is ~6.25 times stronger (model: Mi-6) than the primary [100](010) slip system.

4 Discussion

Our experiments and VPSC modelling reinforces the conclusion that dislocations belonging to the [100](010) slip system are dominant in the deformation of $CaIrO_3$ post-perovskite. This slip system is consistent with that observed in previous studies simple shear studies of $CaIrO_3$ (Walte et al. 2007, Yamazaki et al. 2006), which were preformed at higher temperatures and lower strain-rates. The strength of the EBSD measured texture in our experiment is similar to that measured by Walte et al. (2007) in an experiment to similar total strain and at 1000 °C. This is significantly hotter than our experiment and leads to the conclusion that the differential thermal activation of slip systems in $CaIrO_3$ is not important between 400 °C and 1000 °C.

We have used X-ray diffraction to measure the rate of texture development with applied

strain during simple shear deformation. When combined with VPSC modelling, the data allows us to constrain the relative CRSS of the less active slip systems in $CaIrO_3$ post-perovskite, which have varied wildly in previous studies. The VPSC models that best match to our experimental results have a CRSS for the less active slip systems that is between 4 and 13 times larger than the value used for the most active [100](010) slip system, with a preferred value of 6. The experiment was performed at low temperature (400°C) which is expected to enhance dislocation mediated deformation and suppress deformation mechanisms involving the migration of point defects, even for the small grain sizes exhibited by our samples. Thus our experiment places a likely upper bound on the rate of development of seismic anisotropy with strain.

The pattern of CRSS values predicted for $CaIrO_3$ by Metsue et al. (2009) does not produce the same texture as that inferred from our experiments. Ultimately, the qualitative difference in texture is because either: the CRSS for [001](010) predicted by the Peierls-Nabarro approach is too low, or the CRSS for [100](010) is too high, relative to the other slip systems. We cannot, at present, say which option is more likely but possible causes are variations in the temperature dependence of the CRSS of the different slip systems (caused by differences in kink mobility) or the existence of non-planar dislocation cores for some slip systems. Although these possibilities cannot be examined using the approach adopted by Metsue et al. (2009) more recent modifications to the overall approach (e.g. Cordier et al. 2012, Metsue et al. 2010) which have been applied to other mantle minerals, may offer a way forward. It is interesting to note though, that our preferred secondary CRSS value is much closer to the mean value of the predicted non-primary slip system CRSS in $MgSiO_3$ and $MgGeO_3$ (4.96 and 5.19 respectively), than the value of 50 used in previous modelling by Miyagi et al. (2008). Our experiments on $CaIrO_3$ should be useful for verification of any future modelling of post-perovskite structured minerals, prior to making predictions relevant to $MgSiO_3$ in the lowermost mantle.

Our results imply that the plastic anisotropy of post-perovskite is more similar to olivine than, say, ice and if $MgSiO_3$ behaves like $CaIrO_3$, this result has important implications for models of texture development in the lowermost mantle. For example, the models produced by Walker et al. (2011) all exhibit significantly larger radial anisotropy than that inferred from tomographic inversion (Panning and Romanowicz 2004, 2006, Kustowski et al. 2008) and at least some of this discrepancy may be due to the use of unreasonably large differences in the values for the CRSS of the different slip systems.

To provide a semi-quantitative comparison between our results and observation of seismic anisotropy in the lowermost mantle we have calculated the elastic anisotropy of a polycrystalline aggregate of $MgSiO_3$ post-perovskite with the same texture as that inferred by our diffraction and EBSD data. We use MSAT (Walker and Wookey 2012) and the single crystal elasticity of $MgSiO_3$ post-perovskite at 2800 K and 127 GPa from Wookey et al. (2005b), to calculate the Voigt and Reuss bounds on the elasticity of a sample of 1×10^6 grains drawn from the calculated orientation distribution of $CaIrO_3$. This number of grains was found to be sufficient for there to be less than 0.25 % variation between independent calculations of the anisotropy. In order to make a direct comparison with results from anisotropic tomography and the analysis of Earth's normal modes, we then impose vertical transverse isotropy (VTI) on the sample by taking an average of many replicas of the sample rotated around the normal to the shear plane, which we assume is parallel to the core mantle boundary. We then calculate the phase velocities of vertically (V_{SV}) and horizontally (V_{SH}) polarised shear waves for a horizontally propagating ray and the compressional wave velocity for vertically (V_{PV}) and horizontally (V_{PH}) propagating waves. These values allow us to compute $\xi = V_{SH}^2/V_{SV}^2$ and $\phi = V_{PV}^2/V_{PH}^2$, two commonly reported parameters describing lowermost mantle anisotropy. For the X-ray textures these values are an apparent anisotropy because they include the effects of the 10-element X-ray diffraction detector. To remove this effect we used the fact that the relationship between the

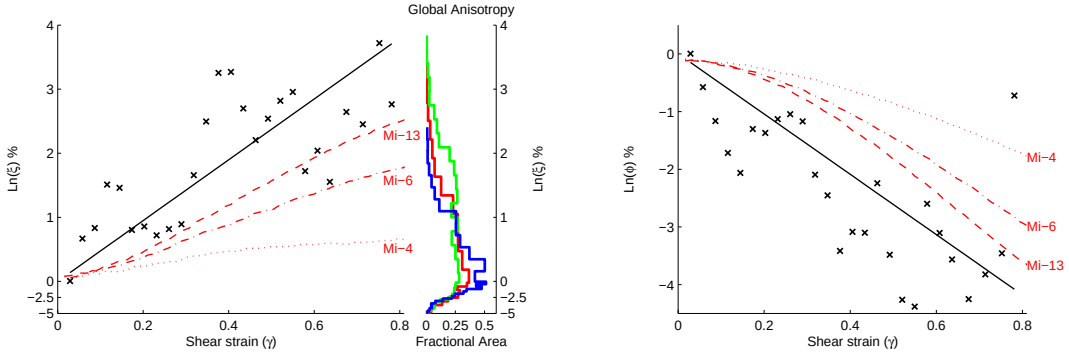

(a) S-anisotropy **(b)** P-anisotropy

Figure 12: (a) S- and (b) P- seismic anisotropies as a function of strain. The black crosses are the experimental values scaled to the raw EBSD value and solid black line a robust linear fit through the origin. The red lines are a selection of the VPSC models. The histograms are the seismic anisotropy, for layer 75 km above the Core-Mantle boundary, in global tomographic models: red - Panning et al. (2010); blue - Panning and Romanowicz (2006); green - Kustowski et al. (2008). Note change in scale for negative values in (a).

seismic anisotropies calculated from the VPSC directly and the modelled VPSC is approximately linear. By assuming the relationship is true for the X-ray data, we scale the seismic anisotropies from the X-ray to those of the EBSD using the values calculated from the modelled EBSD data. Thus enabling a direct comparison between our experimental and global seismic anisotropy data. The EBSD values for $\ln(\xi)$ correspond closest to the model Mi-13 at $\gamma = 0.81$. All the Mi-N models underestimate $\ln(\phi)$ compared to the EBSD data but the Met-N models all have the wrong sign for $\ln(\phi)$. The X-ray data has a greater magnitude of anisotropy than the EBSD value because, as with the texture index, noise in the intensity of the X-ray peaks tends to increase the magnitude of the calculated seismic anisotropies. The rate of increase in $\ln(\xi)$ in the X-ray data is best matched by the model Mi-13 and in $\ln(\phi)$ by the model Mi-6. These rates are consistent with the earlier conclusions that this is the best of the VPSC models investigated here.

In the lowermost mantle, $d\ln(\xi)$ is 2 - 6 % in regions where tomography predicts above average S-wave velocities and is -2 to -4 % in and around the LLSVPs where velocities are low. The anisotropy calculated from the EBSD data has $\ln(\xi) = 2.61$ % (Table 2), which is comparable to the values estimated for the regions in D″ with high S-wave velocities. As these seismically fast areas are interpreted as being cold, they will correspond to the regions where post-perovskite will be most abundant. We focus our discussion on these cold regions as multiple mechanisms have been proposed for the generation of anisotropy in the LLSVPs which are not related to simple shear of post-perovskite with a shear plane parallel to the core-mantle boundary (e.g. Dobson et al. 2011, Ford et al. 2015). The seismic anisotropy measured in our experiment with $\gamma < 1$ matches the largest values measured in the lowermost mantle where the strain is expected to be much larger. This indicates that other processes (such as strain localisation into MgO or diffusion accommodated deformation) are active in the lowermost mantle which reduce the rate of CPO development and/or $MgSiO_3$ post perovskite has less plastic anisotropy than $CaIrO_3$.

Use of inaccurate values for the CRSS used for the various slip systems of post-perovskite is not the only reason why forward models of the generation of seismic anisotropy fail to match, and are often stronger than the anisotropy recovered from seismic observation. A range of other issues make direct comparison between observation and models difficult, and it is notable that

many of these will tend to either increase the strength of the predicted anisotropy or decrease the strength of the anisotropy inferred by observation. On the observational side there is the obvious challenge that strategies for tomographic inversion are designed to produce models that are smooth, and this means that the tomographic model is likely to exhibit lower anisotropy than is really present in the Earth (because roughness that is not supported by the data is suppressed). For models where a parameterisation based on VTI anisotropy is used, this smoothing could be reinforced by averaging observations for rays with different azimuths. A further challenge exists if the anisotropy varies on relatively short length scales. Numerical experiments using finite frequency wave propagation methods show that this tends to result in weaker anisotropy than would be predicted from ray theory given the same anisotropic model of the Earth (Nowacki and Wookey 2016). Deficiencies in polycrystalline models of deformation of the lowermost mantle will also tend to increase the disagreement between forward modelling and observation. For example, current models assume that all deformation is accommodated by dislocation glide and tend to have simplified sets of secondary CRSS values. Grain boundary processes, deformation accommodated by bulk diffusion, or strain partitioning between different phases can all act to decrease rate of texture development. Although modelling techniques that are able to describe these processes exist, we currently lack the experimental data on post-perovskite that would be needed to parameterise them. However, our work indicates choosing CRSS ratios that are consistent with experiment should result in forward models of the development of lowermost mantle anisotropy that are much more consistent with observations than is currently the case.

5 Conclusion

We have demonstrated that it is possible to extract textural information from data measured by an energy-dispersive diffractometer designed to measure stress in deforming samples, even where the sample's crystal structure means that few diffraction peaks can be used. The correspondence between the texture measured using EBSD on the recovered sample and the texture recovered from analysis of the X-ray data suggests that we can use the evolution of texture with strain as a test of models of texture development in $CaIrO_3$ post-perovskite. We note that our method has been made to work for $CaIrO_3$ which has been recovered and subjected to supporting analysis using conventional EBSD. The complexities of the method used serve to highlight the limitations of using energy dispersive XRD to calculate CPO and demonstrate that great care has to be taken to avoid misinterpreting artefacts in the calculated CPO. The need for supporting analysis implies that the method is potentially unsuitable for samples which cannot be recovered from high pressure and temperature (e.g. $CaSiO_3$-perovskite).

Our simple shear experiments indicated that the [100](010) slip system accommodates the majority of the deformation but, to match the rate of texture development, other slip systems must have CRSSs around 6 times greater than that of the primary [100](010) slip system, even under the low temperature conditions of our experiment. If these results are applicable to $MgSiO_3$ post-perovskite in the lower mantle, it appears that part of the mismatch between seismic observations and predictions based on geodynamics and polycrystaline modelling of deformation can be attributed to excessively large differences between the CRSS for different slip systems in $MgSiO_3$. However, the effect of temperature and chemistry on the CRSS for dislocations in post-perovskite structured materials still needs to be fully explored.

Acknowledgements

SAH (NE/H016309/1, NE/L006898/1), AMW (NE/E012922/2, NE/K008803/1) and EM (NE/L007363/1) thank the Natural Environment Research Council for personal fellowships and standard grants. We thank Carlos Tomé and Ricardo Lebensohn for making their VPSC code available to us. Use of the National Synchrotron Light Source, Brookhaven National Laboratory, was supported by the U.S. Department of Energy, Office of Science, Office of Basic Energy Sciences, under Contract No. DE-AC02-98CH10886. Use of the X17B2 beamline was supported by COMPRES, the Consortium for Materials Properties Research in Earth Sciences under NSF Cooperative Agreement EAR 10-43050 and by the Mineral Physics Institute, Stony Brook University. We thank the two anonymous reviewers for useful comments which have improved the manuscript.

References

Ammann, M. W., Brodholt, J. P., Wookey, J., Dobson, D. P., 2010. First-principles constraints on diffusion in lower-mantle minerals and a weak D″ layer. Nature 465, 462 – 465.

Bachmann, F., Hielscher, R., Schaeben, H., 2010. Texture analysis with MTEX–Free and Open Source Software Toolbox. Solid State Phenomena 160, 63–68.

Beghein, C., Trampert, J., van Heijst, H. J., 2006. Radial anisotropy in seismic reference models of the mantle. Journal of Geophysical Research 111, B02303.

Bollinger, C., Merkel, S., Raterron, P., 2012. In situ quantitative analysis of stress and texture development in forsterite aggregates deformed at 6 GPa and 1373 K. Journal of Applied Crystallography 45 (2), 263 – 271.

Boschi, L., Dziewonski, A. M., 2000. Whole Earth tomography from delay times of P, PcP, and PKP phases: Lateral heterogeneities in the outer core or radial anisotropy in the mantle? Journal of Geophysical Research 105, 13675 – 13698.

Carrez, P., Cordier, P., 2010. Modeling dislocations and plasticity of deep Earth materials. In: Wentzcovitch, R. M., Stixrude, L. (Eds.), Theoretical and computational methods in mineral physics: geophysical applications. Vol. 71 of Reviews in Mineralogy and Geochemistry. Mineralogical society of America and the Geochemical Society, Washington DC, Ch. 11, pp. 225 – 252.

Carrez, P., Ferré, D., Cordier, P., 2007a. Implications for plastic flow in the deep mantle from modelling dislocations in $MgSiO_3$ minerals. Nature 446, 68 – 70.

Carrez, P., Ferré, D., Cordier, P., 2007b. Peierls-Nabarro model for dislocations in $MgSiO_3$ post-perovskite calculated at 120 GPa from first principles. Philosophical Magazine 87, 3229 – 3247.

Cordier, P., Amodeo, J., Carrez, P., 2012. Modelling the rheology of MgO under earth's mantle pressure, temperature and strain rates. Nature 481, 117 – 180.

Cottaar, S., Li, M., McNamara, A. K., Romanowicz, B., Wenk, H.-R., 2014. Synthetic seismic anisotropy models within a slab impinging on the core–mantle boundary. Geophysical Journal International 199, 164 – 177.

Dobson, D. P., Hunt, S. A., Lindsay-Scott, A., Wood, I. G., 2011. Towards better analogues for $MgSiO_3$ post-perovskite: $NaCoF_3$ and $NaNiF_3$, two new recoverable fluoride post-perovskites. Physics of the Earth and Planetary Interiors.

Dobson, D. P., McCormack, R., Hunt, S. A., Ammann, M. W., Weidner, D. J., Li, L., Wang, L., 2012. The relative strength of perovskite and post-perovskite in the system $NaCoF_3$. Mineralogical Magazine 76, 925 – 932.

Dobson, D. P., Miyajima, N., Nestola, F., Alvaro, M., Casati, N., Liebske, C., Wood, I. G., Walker, A. M., 2013. Strong inheritance of texture between perovskite and post-perovskite in the D″ layer. Nature Geoscience 6, 575 – 578.

Downs, R. T., Hall-Wallace, M., 2003. The American Mineralogist crystal structure database. American Mineralogist 88, 247 – 250.

Durham, W., Weidner, D., Karato, S., Wang, Y., 2002. New developments in deformation experiments at high pressure. In: Karato, S., Wenk, H. (Eds.), Plastic Deformation of Minerals and Rocks. Vol. 51 of Reviews in Mineralogy & Geochemistry. Mineral. Soc. Am., pp. 21–49.

Ford, H. A., Long, M. D., He, X., Lynner, C., 2015. Lowermost mantle flow at the eastern edge of the African Large Low Shear Velocity Province. Earth and Planetary Science Letters 420, 12 – 22.

Hall, S. A., Kendall, J.-M., van der Baan, M., 2004. Some comments on the effects of lower-mantle anisotropy on SKS and SKKS phases. Physics of the Earth and Planetary Interiors 146, 469 – 481.

He, X., Long, M. D., 2011. Lowermost mantle anisotropy beneath the northwestern Pacific: Evidence from PcS, ScS, SKS, and SKKS phases. Geochemistry Geophysics Geosystems 12, Q12012.

Hielscher, R., Schaeben, H., 2008. A novel pole figure inversion method: specification of the MTEX algorithm. Journal of Applied Crytallography 41, 1024 – 1037.

Hirose, K., Nagaya, Y., Merkel, S., Ohishi, Y., Oct 2010. Deformation of $MnGeO_3$ post-perovskite at lower mantle pressure and temperature. Geophys. Res. Lett. 37 (20), L20302.

Hunt, S. A., Davies, D. R., Walker, A. M., McCormack, R. J., Wills, A. S., Dobson, D. P., Li, L., 2012. On the increase in thermal diffusivity caused by the perovskite to post-perovskite phase transition and its implications for mantle dynamics. Earth and Planetary Science Letters 319 - 320, 96 – 103.

Hunt, S. A., Weidner, D. J., Li, L., Wang, L., Walte, N., Brodholt, J. P., Dobson, D. P., 2009. Weakening of $CaIrO_3$ during the perovskite-post perovskite transformation. Nature Geoscience 2, 794 – 797.

Kendall, J.-M., Silver, P. G., 1996. Constraints from seismic anisotropy on the nature of the lowermost mantle. Nature 381, 409 – 412.

Koelemeijer, P., Deuss, A., Trampert, J., 2012. Normal mode sensitivity to Earth's D″ layer and topography on the core–mantle boundary: what we can and cannot see. Geophysical Journal International 190, 553 – 568.

Kustowski, B., Ekström, G., Dziewoński, 2008. Anisotropic shear-wave velocity structure of the Earth's mantle: a global model. Journal of Geophysical Research 113, B06306.

Lay, T., Young, C. J., 1991. Analysis of seismic SV waves in the core's penumbra. Geophysical Research Letters 18, 1373–1376.

Lebensohn, R. A., Tomé, C. N., 1993. A self-consistent anisotropic approach for the simulation of plastic deformation and texture development of polycrystals: Application to zirconium alloys. Acta Metallurgica et Materialia 41 (9), 2611 – 2624.

Lebensohn, R. A., Tomé, C. N., Ponte Castañeda, P., 2007. Self-consistent modelling of the mechanical behaviour of viscoplastic polycrystals incorporating intragranular field fluctuations. Philosophical Magazine 87, 4287 – 4322.

Lindsay-Scott, A., Wood, I. G., Dobson, D. P., 2007. Thermal expansion of $CaIrO_3$ determined by X-ray powder diffraction. Physics of The Earth and Planetary Interiors 162, 140 – 148.

Long, M. D., 2009. Complex anisotropy in D″ beneath the eastern Pacific from SKS–SKKS splitting discrepancies. Earth and Planetary Science Letters 283, 181 – 189.

Lynner, C., Long, M. D., 2012. Evaluating contributions to SK(K)S splitting from lower mantle anisotropy: A case study from station DBIC, Côte D'Ivoire. Bulletin of the Seismological Society of America 102, 1030 – 1040.

Lynner, C., Long, M. D., 2014. Lowermost mantle anisotropy and deformation along the boundary of the African LLSVP. Geophysical Research Letters 41, 3447 – 3454.

Mainprice, D., Bachmann, F., Hielscher, R., Schaeben, H., 2014. Descriptive tools for the analysis of texture projects with large datasets using MTEX: strength, symmetry and components. In: Faulkner, D. R., Mariani, E., Mecklenburgh, J. (Eds.), Rock Deformation from Field, Experiments and Theory: A Volume in Honour of Ernie Rutter. Vol. 409 of Geological Society of London Special Publication. Geological Society of London.

Martin, D. C., Chapman, K. W., Chupas, P. J., Parakapenka, V., Lee, P. L., Shastri, S. D., Parise, J. B., 2007. Compression, thermal expansion, structure, and instability of $CaIrO_3$, the structure model of $MgSiO_3$ post-perovskite. American Mineralogist 92, 1048 – 1053.

McCormack, R., Dobson, D. P., Walte, N. P., Miyajima, N., Taniguchi, T., Wood, I. G., 2011. The development of shape- and crystallographic-preferred orientation in $CaPtO_3$ post-perovskite deformed in pure shear. American Mineralogist 96 (10), 1630 – 1635.

McDaniel, C. L., Schneider, S. J., 1972. Phase relations in the CaO–IrO_2–Ir system in air. Journal of Solid State Chemistry 4, 274 – 280.

Merkel, S., Kubo, A., Miyagi, L., Speziale, S., Duffy, T. S., Mao, H., Wenk, H.-R., 2006. Plastic deformation of $MgGeO_3$ post-perovskite at lower mantle pressures. Science 311, 644 – 646.

Merkel, S., McNamara, A. K., Kubo, A., Speziale, S., Miyagi, L., Meng, Y., Duffy, T. S., Wenk, H.-R., 2007. Deformation of (Mg,Fe)SiO_3 post-perovskite and D″ anisotropy. Science 316, 1729 – 1732.

Metsue, A., Carrez, P., Denoual, C., Mainprice, D., Cordier, P., 2010. Plastic deformation of wadsleyite: IV Dislocation core modelling based on the Peierls–Nabarro–Galerkin model. Acta Materialia 58, 1467 – 1478.

Metsue, A., Carrez, P., Mainprice, D., Cordier, P., May 2009. Numerical modelling of dislocations and deformation mechanisms in $CaIrO_3$ and $MgGeO_3$ post-perovskites–comparison with $MgSiO_3$ post-perovskite. Physics of the Earth and Planetary Interiors 174 (1-4), 165 – 173.

Miyagi, L., Kanitpanyacharoen, W., Kaercher, P., Lee, K. K. M., Wenk, H.-R., 2010. Slip systems in $MgSiO_3$ post-perovskite: Implications for D″ anisotropy. Science 329 (5999), 1639 – 1641.

Miyagi, L., Kanitpanyacharoen, W., Stackhouse, S., Militzer, B., Wenk, H.-R., 2011. The enigma of post-perovskite anisotropy: deformation versus transformation textures. Physics and Chemistry of Minerals 38, 665 – 678.

Miyagi, L., Nishiyama, N., Wang, Y., Kubo, A., West, D. V., Cava, R. J., Duffy, T. S., Wenk, H.-R., 2008. Deformation and texture development in $CaIrO_3$ post-perovskite phase up to 6 GPa and 1300 K. Earth and Planetary Science Letters 268, 515 – 525.

Miyajima, N., Walte, N., 2009. Burgers vector determination in deformed perovskite and post-perovskite of $CaIrO_3$ using thickness fringes in weak-beam dark-field images. Ultramicroscopy 109, 683 – 692.

Molinari, A., Canova, G. R., Ahzi, S., 1987. A self consistent approach of the large deformation polycrystal viscoplasticity. Acta Metallurgica 35, 2983 – 2994.

Montagner, J.-P., Kennett, B. L. N., 1996. How to reconcile body-wave and normal-mode reference Earth models. Geophysical Journal International 125, 229 – 248.

Morales, L. F., Lloyd, G. E., Mainprice, D., 2014. Fabric transitions in quartz via viscoplastic self-consistent modeling part i: Axial compression and simple shear under constant strain. Tectonophysics 636, 52 – 69.

Murakami, M., Hirose, K., Kawamura, K., Sata, N., Ohishi, Y., 2004. Post-perovskite phase transition in $MgSiO_3$. Science 304, 855 – 858.

Nabarro, F. R. N., 1947. Dislocations in a simple cubic lattice. Proceedings of the Physics Society of London 59, 256 – 272.

Nowacki, A., Walker, A. M., Wookey, J., Kendall, J.-M., 2013. Evaluating post-perovskite as a cause of D″ anisotropy in regions of palaeosubduction. Geophysical Journal International 192, 1085 – 1090.

Nowacki, A., Wookey, J., 2016. The limits of ray theory when measuring shear wave splitting in the lowermost mantle with ScS waves. Submitted to Geophysical Journal International.

Nowacki, A., Wookey, J., Kendall, J.-M., 2010. Deformation of the lowermost mantle from seismic anisotropy. Nature 467, 1091 – 1094.

Nowacki, A., Wookey, J., Kendall, J.-M., 2011. New advances in using seismic anisotropy, mineral physics and geodynamics to understand deformation in the lowermost mantle. Journal of Geodynamics 52, 205 – 228.

Oganov, A. R., Ono, S., 2004. Theoretical and experimental evidence for a post-perovskite phase of $MgSiO_3$ in the Earth's D″ layer. Nature 430, 445 – 448.

Ohuchi, T., Kawazoe, T., Nishiyama, N., Yu, N., Irifune, T., 2010. Technical development of simple shear deformation experiments using a deformation-dia apparatus. Journal of Earth Science 21 (5), 523–531.

Okada, T., Yagi, T., Niwa, K., Kikegawa, T., 2010. Lattice-preferred orientations in post-perovskite-type mggeo3 formed by transformations from different pre-phases. Physics of the Earth and Planetary Interiors 180 (3-4), 195 – 202.

Panning, M., Romanowicz, B., 2004. Inferences on flow at the base of Earth's mantle based on seismic anisotropy. Science 303, 351 – 353.

Panning, M., Romanowicz, B., 2006. A three-dimensional radially anisotropic model of shear velocity in the whole mantle. Geophysical Journal International 167, 361 – 379.

Panning, M. P., Leki, V., Romanowicz, B. A., 2010. Importance of crustal corrections in the development of a new global model of radial anisotropy. Journal of Geophysical Research 115 (B12).

Peierls, R., 1940. The size of a dislocation. Proceedings of the Physics Society of London 52, 34 – 37.

Rodi, F., Babel, D., Mar 1965. Ternäre oxide der übergangsmetalle. IV. Erdalkaliiridium(IV)-oxide: Kristallstruktur von $CaIrO_3$. Zeitschrift für anorganische und allgemeine Chemie 336 (1-2), 17 – 23.

Rokosky, J. M., Lay, T., Garnero, E. J., 2006. Small-scale lateral variations in azimuthally anisotropic D″ structure beneath the Cocos Plate. Earth and Planetary Science Letters 248, 411 – 425.

Singh, A. K., Balasingh, C., Mao, H.-k., Hemley, R. J., Shu, J., 1998. Analysis of lattice strains measured under nonhydrostatic pressure. Journal of Applied Physics 83 (12), 7567.

Soldati, G., Boschi, L., Piersanti, A., 2003. Outer core density heterogeneity and the discrepancy between PKP and PcP travel time observations. Geophysical Research Letters 30, 1190.

Stølen, S., Trønnes, R. G., 2007. The perovskite to post-perovskite transition in $CaIrO_3$: Clapeyron slope and changes in bulk and shear moduli by density functional theory. Physics of the Earth and Planetary Interiors 164 (1–2), 50 – 62.

Vinnik, L., Romanowicz, B., Le Stunff, Y., Makeyeva, L., 1995. Seismic anisotropy in the D″ layer. Geophysical Research Letters 22, 1657 – 1660.

Walker, A. M., Carrez, P., Cordier, P., 2010. Atomic-scale models of dislocation cores in minerals: progress and prospects. Mineralogical Magazine 74, 381 – 413.

Walker, A. M., Forte, A. M., Wookey, J., Nowacki, A., Kendall, J.-M., 2011. Elastic anisotropy of D″ predicted from global models of mantle flow. Geochem. Geophys. Geosyst. 12, Q10006.

Walker, A. M., Wookey, J., 2012. MSAT — A new toolkit for the analysis of elastic and seismic anisotropy. Computers & Geosciences 49, 81–90.

Walte, N., Heidelbach, F., Miyajima, N., Frost, D. J., 2007. Texture development and TEM analysis of deformed $CaIrO_3$: Implications for the D″ layer at the core-mantle boundary. Geophysical Research Letters 34, L08306.

Walte, N. P., Heidelbach, F., Miyajma, N., Frost, D. J., Rubie, D. C., Dobson, D. P., 2009. Transformation textures in post-perovskite: Understanding mantle flow in the D″ layer of the Earth. Geophysical Research Letters 36, L04302.

Wang, Y., Durham, B., Getting, I. C., Weidner, D. J., 2003. The deformation-DIA: A new apparatus for high temperature triaxial deformation to pressures up to 15GPa. Review of Scientific Instruments 74 (6), 3002 – 3011.

Weidner, D. J., Vaughan, M. T., Wang, L., Long, H., Li, L., Dixon, N. A., Durham, W. B., 2010. Precise stress measurements with white synchrotron X-rays. Review of Scientific Instruments 81, 013903.

Wenk, H.-R., Cottaar, S., Tomé, C. N., McNamara, A., Romanowicz, B., 2011. Deformation in the lowermost mantle: From polycrystal plasticity to seismic anisotropy. Earth and Planetary Science Letters 306, 33 – 45.

Wookey, J., Kendall, J.-M., 2008. Constraints on lowermost mantle mineralogy and fabric beneath Siberia from seismic anisotropy. Earth and Planetary Science Letters 275, 32 – 42.

Wookey, J., Kendall, J.-M., Rümpker, G., 2005a. Lowermost mantle anisotropy beneath the north Pacific from differential *S*–*ScS* splitting. Geophysical Journal International 161, 829 – 838.

Wookey, J., Stackhouse, S., Kendall, J.-M., Brodholt, J., Price, G. D., 2005b. Efficacy of the post-perovskite phase as an explanation for lowermost-mantle seismic properties. Nature 438 (7070), 1004 – 1007.

Wright, I. S., Nowell, M. M., Bingert, F. J., 2007. A comparison of textures measured using X-ray and electron backscatter diffraction. Metallurgical and Materials Transactions A 38 (8), 1845–1855.

Yamazaki, D., Yoshino, T., Ohfuji, H., Ando, J.-i., Yoneda, A., 2006. Origin of seismic anisotropy in the D″ layer inferred from shear deformation experiments on post-perovskite phase. Earth and Planetary Science Letters 252, 372 – 378.

Supplementary Information for:

In-situ measurement of texture development rate in $CaIrO_3$ post-perovskite

Simon A. Hunt, Andrew M. Walker, Elisabetta Mariani

Figure S1: Inverse pole figures of Met-N VPSC models as a function of strain

VPSC step	Strain (γ)	Met-62	Met-31	Met-16
10 of 50	0.162	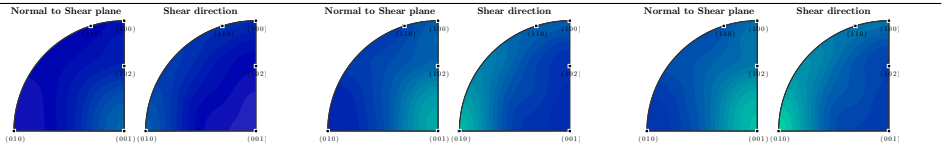		
20 of 50	0.324	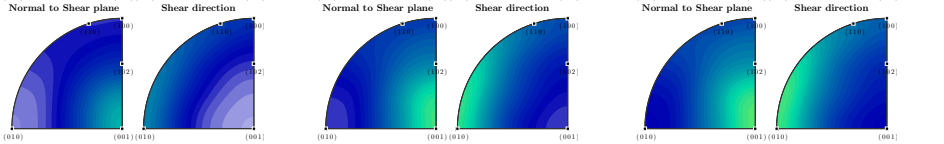		
30 of 50	0.486	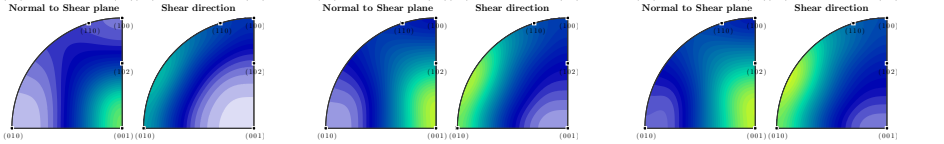		
40 of 50	0.648	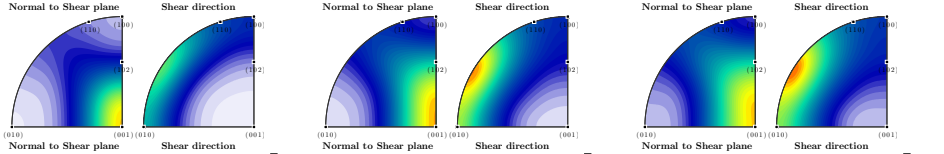		
50 of 50	0.810	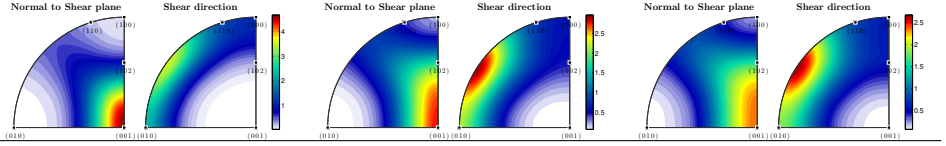		

Figure S2: Inverse pole figures of Mi-N VPSC models as a function of strain

VPSC step	Strain (γ)	Mi-50	Mi-25	Mi-13	Mi-6	Mi-4
10 of 50	0.162	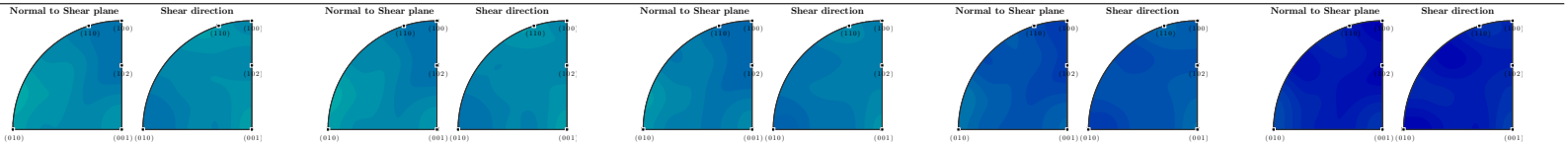				
20 of 50	0.324	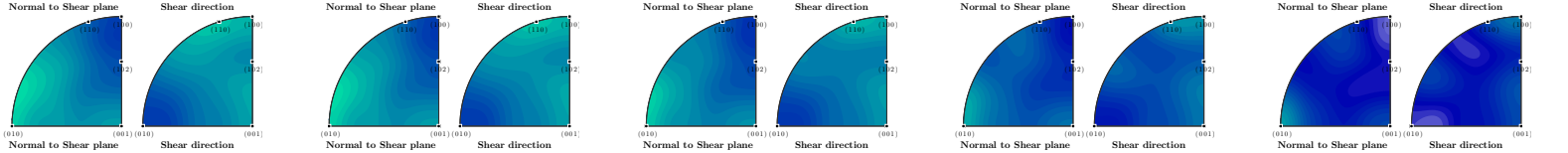				
30 of 50	0.486	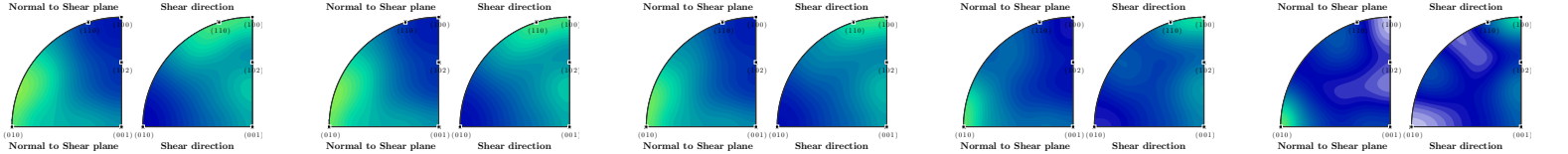				
40 of 50	0.648	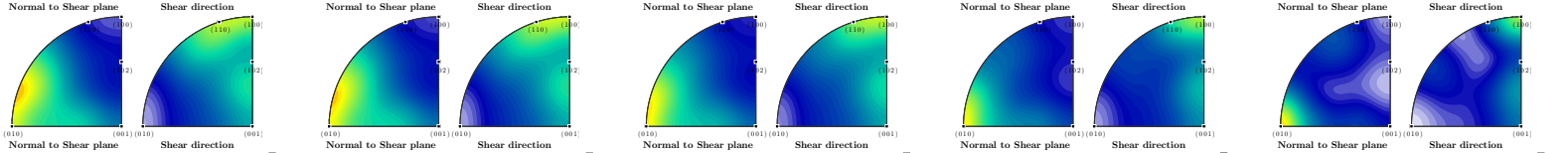				
50 of 50	0.810	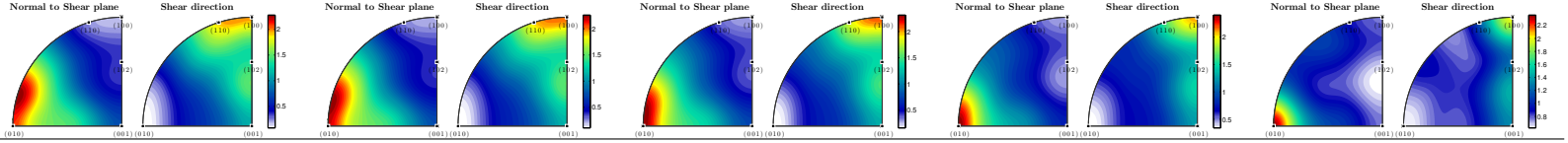				

Figure S3: Inverse pole figures of Mi-N-nn VPSC models as a function of strain

VPSC step	Strain (γ)	Mi-13-n2	Mi-13 (n = 3)	Mi-13-n5
10 of 50	0.162	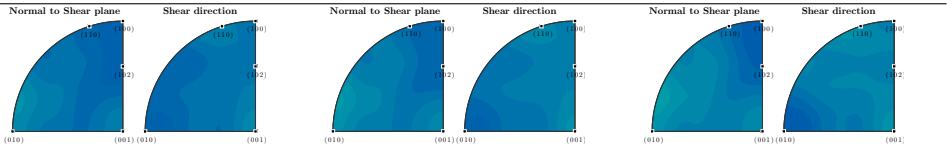		
20 of 50	0.324	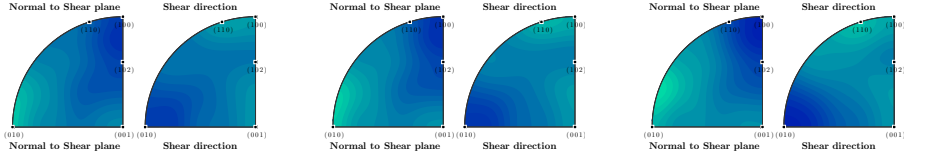		
30 of 50	0.486	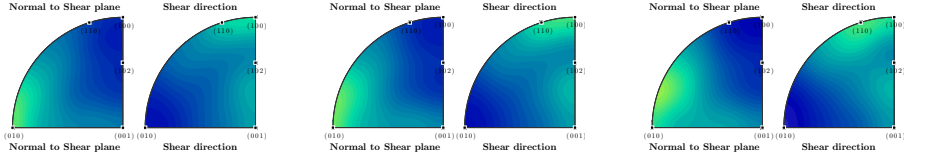		
40 of 50	0.648	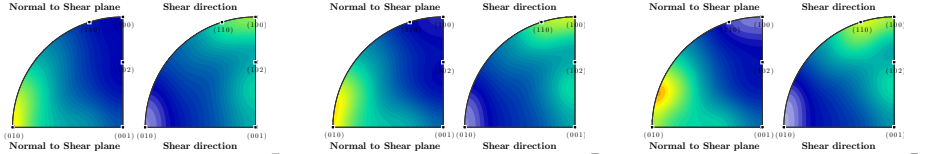		
50 of 50	0.810